Nitrogen treatment generates tunable nanohybridization of Ni_5P_4 nanosheets with nickel hydr(oxy)oxides for efficient hydrogen production in alkaline, seawater and acidic media

Yongchao Huang[b,1], Lei Hu[c,1], Ran Liu[d], Yuwen Hu[c], Tuzhi Xiong[a], Weitao Qiu[c], M.-Sadeeq (Jie Tang) Balogun[a,*], Anlian Pan[a,*], Yexiang Tong[c,*]

[a] College of Materials Science and Engineering, Hunan University, Changsha 410082, Hunan, People's Republic of China
[b] Institute of Environmental Research at Greater Bay, Key Laboratory for Water Quality and Conservation of the Pearl River Delta, Ministry of Education, Guangzhou University, Guangzhou 510006, People's Republic of China
[c] MOE of the Key Laboratory of Bioinorganic and Synthetic Chemistry, The Key Lab of Low-Carbon Chemistry & Energy Conservation of Guangdong Province, School of Chemistry, Sun Yat-sen University, Guangzhou 510275, People's Republic of China
[d] Division of Engineering Science, Faculty of Applied Science & Engineering, University of Toronto, St. George (Downtown Toronto) Campus, 27 King's College Cir, M5S, Toronto, ON, Canada

ARTICLE INFO

ABSTRACT

Hybrid engineering of electrocatalysts is still very challenging for electrochemical water splitting. Ni_5P_4 is a promising electrocatalyst for hydrogen evolution reaction (HER) but the formation of phosphide-hydrogen on Ni_5P_4 (P-H_{ads}) bonds usually weakens the HER activity. Herein, we report a simple nitrogen treatment strategy to controllably hybridize Ni_5P_4 porous nanosheets with amorphous nickel hydr(oxy)oxide [$Ni^{2+\delta}O_8(OH)_{2-\delta}$] layer and utilize as efficient electrocatalyst for hydrogen evolution reaction (HER) in neutral (real seawater), alkaline and acidic media. The in situ derived $Ni_5P_4@Ni^{2+\delta}O_8(OH)_{2-\delta}$ hybrid nanosheets can be obtained by annealing the nickel hydroxide-precursor nanosheets coupled with decomposition of $NaH_2PO_2·H_2O$ in nitrogen atmosphere. Benefiting from the thin amorphous $Ni^{2+\delta}O_8(OH)_{2-\delta}$ coated layer, the optimized $Ni_5P_4@Ni^{2+\delta}O_8(OH)_{2-\delta}$ with 3 nm amorphous layer achieve a current density of 10 mA cm^{-2} at low overpotential of 87, 144 and 66 mV in alkaline, seawater and acidic media, respectively. Theoretical and experimental analyses show that the hybridization of Ni_5P_4 and $Ni^{2+\delta}O_8(OH)_{2-\delta}$ could not only serve as protection to further enhance the electrocatalytic properties and high surface area of the hybrid electrocatalyst but also create good electronic interaction and synergistic properties for suppressing P-H_{ads} bonds, which is beneficial for promoting water adsorption and optimizing the free energy of hydrogen adsorption for triggering the catalytic pathway at all pH range. This work offers new insights for facile designing of non-precious transition metal compound hybrids for HER with enhancing electrocatalytic performance and opens a promising pathway for hydrogen production at all-pH range.

1. Introduction

One of the most promising alternative fuels is hydrogen because it has a high gravimetric energy density, and is renewable and clean [1,2]. Thus, producing hydrogen through hydrogen evolution reaction (HER) from water did not only require the development of cost-effective and efficient electrocatalysts [3–5] but also demand for electrocatalysts that can work at different pH conditions [6–10]. Pt-based materials remain suitable electrocatalysts that can operate efficiently at

different pH but are limited by the problem of high-cost, scarcity and stability. Therefore, it is highly important to develop new electrocatalysts that will not only possess similar catalytic properties like that of Pt or better than Pt but could also operate effectively at wide pH-range.

Currently, transition metal phosphides such as nickel phosphides have been proven to be more efficient for catalyzing the HER by both computational and experimental studies [1,11–17]. Among them, Ni_5P_4 has recently gained attention as better electrocatalyst for hydrogen

---

* Corresponding authors.
E-mail addresses: balogun@hnu.edu.cn (M.-S.J.T. Balogun), anlian.pan@hnu.edu.cn (A. Pan), chedhx@mail.sysu.edu.cn (Y. Tong).
[1] These authors contributed equally to this work.

evolution in both acidic and alkaline media than other Ni phosphide-based catalysts [18–22]. However, theoretical analysis has shown that a phosphide-hydrogen (P-H$_{ads}$) bond is formed during HER and the H atoms adsorbed point is in the direction of the P$_3$-hollow site of Ni$_5$P$_4$ [23,24]. With increase of the H atoms in the P$_3$-hollow site, the P-P-H bonding angle increases, and this destabilizes the H adsorption leading to unsatisfactory HER activity [23]. To promote the H adsorption in Ni$_5$P$_4$, the electronic density distributions in Ni$_5$P$_4$ require modification so as to weaken the P-H$_{ads}$ bonds [25].

Another strategy to modify and optimize the electrocatalytic performances of electrocatalysts is surface engineering through hybridization [26–35]. Nanohybridization of electrocatalysts have explicated that there usually exist an electronic interaction between two compounds, [36,37] which leads to synergistic hybrid catalyst system that could alter the charge distribution in the hybrid electrocatalyst [38] and is also beneficial for optimizing adsorption through lowering free energy of H [27,39–41]. In search of suitable electrocatalyst for hybridization, it is highly important to note that hydroxides and hydr(oxy)oxides are robust electrocatalysts that are capable of binding and adsorbing hydroxyl (OH) species as well as catalyzing water dissociation [42–45]. They have been used as OH acceptor to facilitate HER processes with rich hydrogen acceptor transition metal compounds (TMCs) [40,46]. A common approach to the hybridization of hydroxides and hydr(oxy)oxides with TMCs involves two-steps whereby the hydroxides and hydr(oxy)oxides separately react with the pristine electrocatalysts [47–49]. Despite the enhanced catalytic performance reported by this approach, further development of simpler or one-step strategy for the design of nanohybrid electrocatalysts is necessary.

In this work, we develop a hybrid electrocatalyst that consists of hydrogen acceptor Ni$_5$P$_4$ and hydroxyl acceptor amorphous nickel hydr(oxy)oxide [Ni$^{2+\delta}$O$_8$(OH)$_{2-\delta}$] via a simple treatment of Ni precursor in nitrogen gas (N$_2$) atmosphere to facilitate enhanced HER activity. The as-prepared NPNNS hybrid is not only highly active as HER electrocatalyst in alkaline media but also displays attractive performance toward HER in real seawater (neutral electrolyte). The optimal NPNNS exhibited overpotential of 87, 144 and 66 mV at the current density of 10 mA cm^{-2} and low Tafel slope of 69, 108 and 33 mV dec^{-1} in alkaline, real seawater and acidic electrolytes, respectively. The overall HER performance of the optimal NPNNS electrocatalysts is superior to most of the reported Ni$_5$P$_4$-based and comparable to commercial Pt/C. The excellent performance of NPNNS can be related to the higher specific surface area, synergistic effect and electronic interaction between the phosphide and hydr(oxy)oxide that brings about high catalytic efficiency and excellent durability.

2. Experimental

2.1. Synthesis of NPNNS

Ni(NO$_3$)$_2$·6H$_2$O, hexamethylenetetramine (HMT) and sodium hypophosphite (NaH$_2$PO$_2$·H$_2$O, NHP) were purchased from Guangzhou Chemical Reagent Factory, Guangzhou, China. All chemicals were directly used without further purification. In a typical synthesis, 20 mmol Ni(NO$_3$)$_2$·6H$_2$O and 40 mmol HMT were dissolved in 70 mL deionized water under vigorous stirring for 30 min. During the stirring process, carbon cloth (CC) (purchased from Fuel Cell Earth LLC, United States) was carefully and thoroughly cleaned with concentrated nitric acid, and then washed with deionized water, acetone and ethanol several times. Next, the cleaned CC (4 cm × 6 cm) was immersed in the above solution, transferred to an 80 mL Teflon-lined stainless steel autoclave and heated at 120 °C for 12 h. The autoclave was allowed to cool to room temperature, and the sample was gently removed from the autoclave. The CC was coated with green films of the Ni-hydroxide precursor [Ni(OH)$_2$·0.75H$_2$O], washed with water and ethanol, and dried in a 60 °C oven overnight. Ni(OH)$_2$·0.75H$_2$O was then placed in a tube furnace with 200 mg NHP and heated to 380 °C for 3 h at a ramping rate of

10 °C min^{-1} and flow rate of 450 sccm under a N$_2$ atmosphere. The purity of the N$_2$ gas is 99.999%. The furnace was allowed to cool to room temperature under a N$_2$ flow, and the final products were collected and denoted as NPNNS.

2.2. Synthesis of NPONS

Ni(OH)$_2$·0.75H$_2$O was also annealed in Ar atmosphere with 200 mg NHP and heated to 380 °C for 3 h at a ramping rate of 10 °C min^{-1} and flow rate of 450 sccm. The purity of the Ar gas is 99.999%. The obtained product obtained was denoted as NPONS.

2.3. Synthesis of NONNS

Ni(OH)$_2$·0.75H$_2$O was also annealed in N$_2$ atmosphere without NHP and heated to 380 °C for 3 h at a ramping rate of 10 °C min^{-1} and flow rate of 450 sccm. The product obtained was denoted as NONNS.

2.4. Sample characterization

The crystal structures were determined by X-ray diffraction (XRD; Shimadzu X-ray diffractometer 6000, Cu K$_\alpha$ radiation, Shimadzu, Tokyo, Japan). The scan speed was 2° min^{-1}. Field emission scanning electron microscopy (FESEM, Quanta 400/INCA/HKL) was used to study the morphologies of the samples. Insight morphology and elemental mapping analysis were carried out using a transmission electron microscope (TEM) (F30). X-ray photoelectron spectroscopy (XPS, ESCALab250, Thermo VG) was used to confirm the electronic interaction, composition and chemical states of the elements in the samples. Raman spectroscopy was performed using a laser micro-Raman spectrometer (Renishaw inVia) at room temperature with an Ar$^+$ laser and 514.5 nm excitation. The nitrogen adsorption–desorption isotherms used to determine the specific surface area were measured using a Micromeritics ASAP 2000 system at 77 K.

2.5. Electrochemical characterization

The electrochemical measurements were performed using a three-electrode system on an electrochemical workstation (CHI760E). The above synthesized samples were used as the working electrodes, carbon rod as the counter electrode and Ag/AgCl (saturated solution) as the reference electrode. The geometric area of the samples was determined as the active area. The samples used for the electrochemical tests were sealed with an epoxy resin, leaving a 1 cm × 1 cm in area square for measuring and a small area at the other end for ohmic contact. The overpotential values used for the HER study were also calculated according to the following equation: E (RHE) = E (Ag/AgCl) + 0.197 + 0.059*pH. The Tafel plots were measured at 10 mV s^{-1}, and the Tafel slopes were calculated based on the equation: η = b log j + a, where η, b and j are the overpotential, Tafel slope and current density, respectively. Electrochemical impedance spectroscopy (EIS) measurements were performed from 100 MHz to 0.01 Hz at overpotential of 100 mV.

For comparison, a commercial 20% Pt/C on CC (denoted Pt/C-CC) as working electrode and test it under the same condition as other HER catalysts. About 2 mg of Pt/C was ultrasonically dispersed in a mixture of 1 mL water and 30 μL of 0.1% Nafion. Finally, the catalyst dispersion was transferred onto CC and dried overnight. The geometric area of the Pt/C-CC was 1 cm × 1 cm.

2.6. Gas chromatography measurements

The amount of H$_2$ gas evolved was measured by an in situ gas chromatography system (BEIJING PERSEE, G5) using Pt for the calibration. The electrolysis was performed at overpotential of 130 mV for 3600 s in 40 mL of the various electrolytes at ambient temperature

(1 atm). The amount of H_2 gas was recorded every 1200 s.

2.7. DFT calculations

All the calculations were performed based on spin-polarized periodic density functional theory (DFT) implemented in Gaussian 09W [50]. The calculation basis set was B3LYP and the total energy convergence was set to be lower than 10^{-5} eV, and the force convergence was set to be smaller than 0.02 eV/Å. The potential of all the calculations was set to 0 V. The Gibbs free energy change (ΔG) of each reaction step is calculated as:

$$\Delta G = E_{tot(b)} - E_{tot(a)} + \Delta E_{ZPE} - T\Delta S$$

where $E_{tot(b)}$ is the energy of the given unit cell with intermediate of the latter state, $E_{tot(a)}$ is the energy of the intermediate of the previous state, ΔE_{ZPE} is the difference corresponding to the zero point energy change between the intermediates of the previous state and the latter state, ΔS is entropy change between the intermediates of the previous state and the latter state, T represents the temperature applied for HER.

3. Results

### 3.1. Synthesis and morphological characterization

NPNNS were synthesized via nitrogen treatment of the hydrothermally prepared $Ni(OH)_2 \cdot 0.75H_2O$ precursor nanosheets (details in Section 2). The formation of NPNNS catalyst can be related to the decomposition of NHP to form PH_3, which can be absorbed at the Ni-hydroxide precursor surface to form Ni_5P_4, followed by the reaction of the gaseous H_2O with N_2 gas to achieve the coated amorphous layer (Scheme 1). Firstly, $Ni(OH)_2 \cdot 0.75H_2O$ precursor nanosheets (Supplemtental Material-Figure S1a) were grown on a free-standing carbon cloth via a hydrothermal reaction as reported in our previous work [51]. Scanning electron microscopy (SEM) images of the $Ni(OH)_2 \cdot 0.75H_2O$ show a uniform coating of the nanosheets on the carbon cloth fibers (Figure S1b) with a diameter of approximately 40 nm (Figure S1c). The precursors were then annealed in Ar and N_2 atmosphere at 380 °C in the presence of NHP for 180 min at a flow rate of 400 sccm (Scheme 1). The X-ray diffraction (XRD) patterns in Figure S2 show that both samples have peaks from the Ni_5P_4 phase (PDF#18-0883), which confirmed the successful formation of Ni_5P_4. However, the intensity of Ar-treated sample is higher than that of N_2-treated sample, suggesting better crystallinity of the former sample than the latter sample. Uniform coating of the nanosheets on the carbon cloth substrate was maintained in both NPONS (Figure S3a) and NPNNS (Figure S4) after the annealing process, and the nanosheets become rough and porous (Figures S3b and 1a). N_2-absorption isotherms and pore-width distributions show the Brunauer–Emmett–Teller (BET) specific surface area and pore sizes of NPNNS are 147.32 $m^2 g^{-1}$ and 33.86 $cm^3 g^{-1}$, respectively, which are higher than the NPONS counterpart (91.14 $m^2 g^{-1}$ and 21.54 $cm^3 g^{-1}$) (Figure S5). The morphologies of NPONS and NPNNS were further observed by transmission electron microscopy (TEM). High-resolution TEM (HRTEM) image collected from the surface of NPONS nanosheets (Figure S6) revealed lattice fringes of 0.55 nm, corresponding to (002) phase of Ni_5P_4 (Fig. 1b inset). For NPNNS sample, a lattice spacing of

Figures

Scheme 1. Schematic illustration of NPNNS hybrid nanosheets.

0.58 nm that corresponds to the (100) phase of hexagonal Ni_5P_4 (PDF#18-0883) was also revealed (Fig. 1c inset). Interestingly, NPNNS is decorated with a 3 nm thin amorphous layer was formed on its surface (Fig. 1c), while the surface of NPONS is smooth (Fig. 1b).

To determine the composition of the coated layer, electron energy-loss spectroscopy (EELS) and energy dispersive X-ray spectrum (EDS) were employed. According to the EELS images obtained from the HAADF spectrum in Fig. 1d, both the Ni (green) and P (red) are uniformly distributed, while a thin O layer (yellow) can also be observed at the surfaces, suggesting the presence of an oxide layer. EDS spectra derived from the coated layer (represented as O_1) and inner layer (represented as O_2) of the NPNNS (Fig. 1e inset) reveals that the relative intensity (number of counts) of Ni and P at the outer layer is very low compared to the inner layer, while that of O layer of the former is almost the same with that of the latter (Fig. 1e). However, the Ni:P:O atomic ratio of the outer layer is 53:36:11 (i.e. P/O ratio is 3.27:1) and that of the inner layer is 44:53:3 (i.e. P/O ratio is 17.67:1). These results suggest that the outer coated layer could be an amorphous layer of nickel oxide.

3.2. Electronic state and interaction characterization

X-ray photoelectron spectroscopy (XPS) analyses of NPONS, NONNS and NPNNS were performed to determine the electronic state of the samples (Fig. 2). In Fig. 2a, the binding energy (eV) of Ni^{2+} peak associated with Ni_5P_4 in NPONS ($2p_{3/2}$) [20] positively shifted to the higher binding energy after formation of the amorphous layer. Ni^{2+} peak of nickel oxide in NONNS [29,52] also shifted to higher binder energy after NPNNS formation, further confirming oxidation of nickel oxide ($Ni^{2+\delta}O_\delta$) (Fig. 2b) [46,53]. However, Ni^{2+} peak of nickel oxide in NPNNS exhibited high intensity than that of NPONS (Fig. 2a). We suggested that such high intensity in NPNNS can be associated with the formation of amorphous nickel oxide layer, while the Ni^{2+} peak of nickel oxide in NPONS can be related with the sample expose to air. On the other hand, the Ni^{2+} peak of Ni_5P_4 in NPONS and NPNNS are almost the same, suggesting similar electronic state in both samples. However, the intensity of Ni_5P_4 Ni^{2+} peak of NPNNS is lower than that of NPONS (Fig. 2a). The reason might be attributed to the formation of amorphous layer in the hybrid sample, which could suppress the crystallinity of Ni_5P_4 peaks, and also in conform to the XRD results (Figure S2). It can be observed that Raman spectra in Fig. 2c shows a broad band around 465 cm^{-1}, which is consistent with the $A_{1g(T)}$ mode due to Ni-OH, confirming the formation of hydroxide in NPNNS hybrid sample [46,54,55]. The P $2p_{1/2}$ spectra of NPONS exhibited a negative shift to the lower binding energy after formation of NPNNS hybrid (Fig. 2d). Such positive and negative shifts identify an electronic interaction between the P-sites of Ni_5P_4 and Ni-sites of both Ni_5P_4 and $Ni^{2+\delta}O_\delta(OH)_{2-\delta}$. Additionally, O 1s XPS spectra of NPNNS is characterized with Ni-O (530.0 eV), OH^- (531.6 eV) and PO_x (532.7 eV) peaks (Fig. 2e-ii), corresponding to oxide [56–58], hydroxide [42,46,54,55] and phosphate [59,60], respectively. These peaks are totally weak in NPONS (2e-i). Furthermore, the peak at 130.8 eV in P 2p XPS spectra of NPNNS also affirmed the oxide layer formation [59,60]. Hence, with the oxidation of Ni in NPNNS and the presence of both oxide and hydroxide, we confirm that the amorphous layer on Ni_5P_4 nanosheets is nickel hydr(oxy)oxide $[Ni^{2+\delta}O_\delta(OH)_{2-\delta}]$ [53]. The electronic interaction could allow nickel hydr(oxy)oxide to improve the performance of Ni_5P_4 through "nanohybridization" and "metal-metal interaction" becuase previous works have shown that nanohybridization usually occurs when metal or metallic-like or hydroxide or oxyhydroxide materials hybridized with another transition metal compounds [27,33,40,50]. It can be observed in Fig. 2f that all the Raman peaks for NPONS correspond to the Ni-P bonds of Ni_5P_4 [20]. Compared with that of NPNNS, the entire Raman peaks exhibit red-shifts further confirming electronic interaction between Ni_5P_4 and $Ni^{2+\delta}O_\delta(OH)_{2-\delta}$. Hence, we proposed possible reaction for the formation of the Ni_5P_4 and
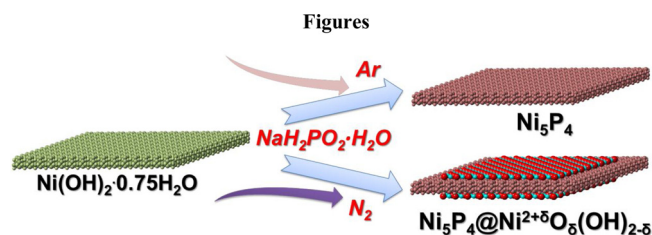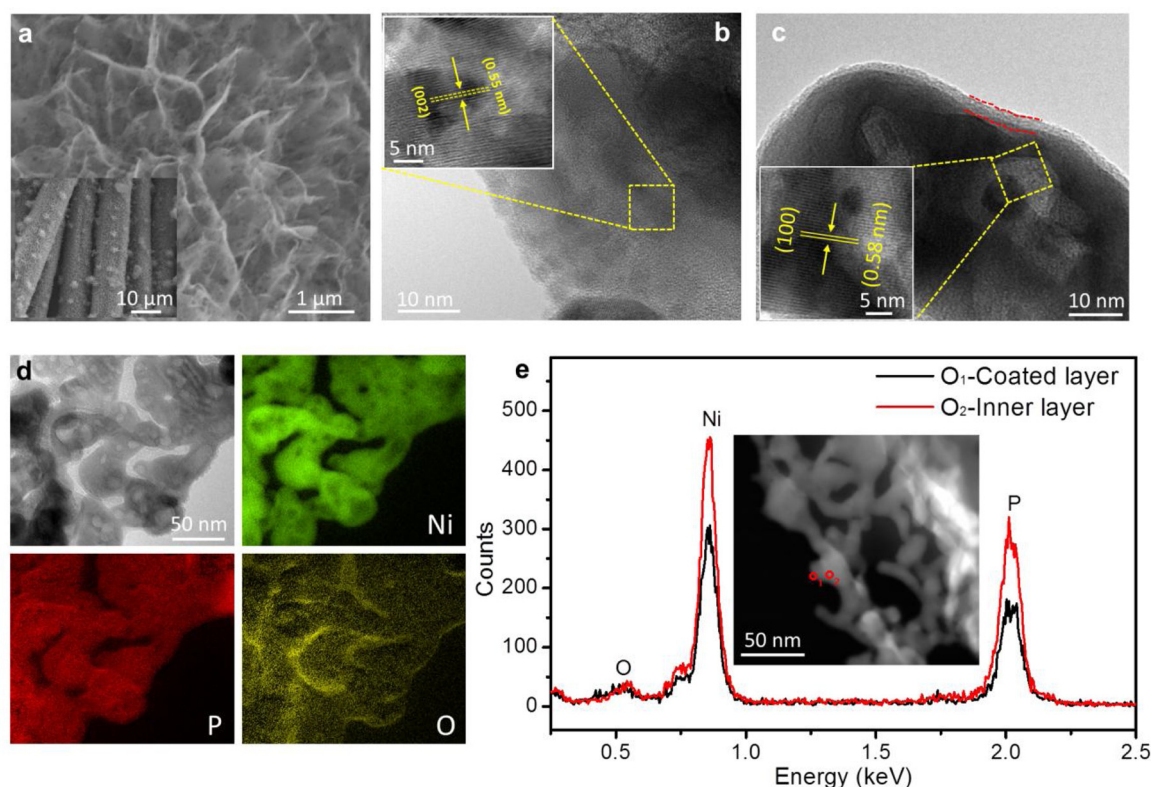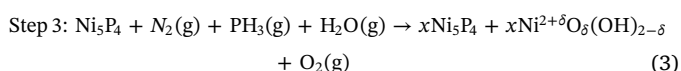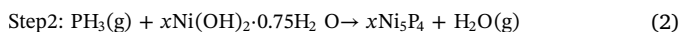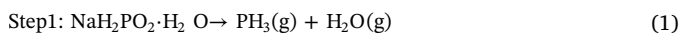
Fig. 1. (a) SEM image of NPNNS. HRTEM images of (b) NPONS and (c) NPNNS. Inset is the HRTEM image displaying their corresponding lattice fringes. (d) EELS images of NPNNS. (e) EDX spectra obtained from the core and shell area of the NPNNS catalyst. Inset is the HAADF image indicating the points (O_1 and O_2) where the EDX data were obtained.

hydro(oxy)oxide layer as shown in Eqs. (1)–(3)

Step1: $NaH_2PO_2 \cdot H_2 O \rightarrow PH_3(g) + H_2O(g)$ (1)

Step2: $PH_3(g) + xNi(OH)_2 \cdot 0.75H_2 O \rightarrow xNi_5P_4 + H_2O(g)$ (2)

Step 3: $Ni_5P_4 + N_2(g) + PH_3(g) + H_2O(g) \rightarrow xNi_5P_4 + xNi^{2+\delta}O_\delta(OH)_{2-\delta}$
$$+ O_2(g) \qquad (3)$$

In step 1 (Eq. (1)), upon heating the furnace above 100 °C, NHP melted along with the release of PH_3 gas as well as the evaporation of the water of crystallization of $xNi(OH)_2 \cdot 0.75H_2O$ as the temperature increases up to 380 °C, Ni_5P_4 is formed as seen in step 2 (Eq. (2)). At this temperature, the furnace is maintained for longer period of time with the flow of N_2 gas at 400 sccm. Gradually, according to step 3, long-time reaction of the N_2 gas could react with the water vapor to form O_2 (g) and NH_3 (g), which further reacted with Ni_5P_4 and oxidized the surface of Ni_5P_4 forming an amorphous $Ni^{2+\delta}O_\delta(OH)_{2-\delta}$ layer (eq. 3). Moreover, further XPS analysis shows that that N can be found in NPNNS hybrid, which are mainly pyridinic and pyrrolic N, and also confirming N-doping (Figure S5c)

3.3. Tunable hybrid formation

Further insight on the $Ni^{2+\delta}O_\delta(OH)_{2-\delta}$ shell was studied based on NHP mass (mg), N_2 annealing flow rate (sccm) and annealing duration (min). Details about the engineering can be found in Table S1–S3. Firstly, the Ni-precursor was subjected to N_2 annealing at two different flow rate of 225 sccm (denoted as NPN-1) and 450 sccm (denoted as NPN-2 or NPNNS), maintaining the annealing time at 180 min and NHP mass at 200 mg. XRD shows a weak signal of Ni_2P for NPN-1 and Ni_5P_4 for NPNNS (Figure S7a), suggesting that the flow rate could be used to tune Ni-P phases. TEM images display that both NPN-1 and NPNNS were coated with orderly thin layer of $Ni^{2+\delta}O_\delta(OH)_{2-\delta}$ (Figure S7b and

S7d), respectively. Also, HRTEM reveals that the NPN-1 coated layer has a uniform diameter of 2.2 nm (Figure S7c), while that of NPN-2 is 3 nm (Figure S7e). Secondly, compared with that of NPN-2, the Ni-precursor was also annealed along with different desired NHP mass of 50 and 100 mg to obtain the NPN-3 and NPN-4, respectively with a fixed N_2 flow rate at 450 sccm and annealing time (180 min). XRD measurement confirmed Ni_5P_4 phase for NPN-2 and NPN-4, while that of NPN-3 is mainly Ni_2P phase (Figure S8a). This result also indicated that the mass of NHP can also be used to determine different Ni-P phases. According to TEM (Figure S8b) and HRTEM (Figure S8c) images of the NPN-3 sample, no $Ni^{2+\delta}O_\delta(OH)_{2-\delta}$ coated layer can be found. However, the NPN-4 consist of uniform coated layer (Figure S8d) with a thickness of 2 nm (Figure S8e), revealing that the nickel oxide shell layer is also dependent of the NHP mass. Furthermore, we studied the effect of annealing time (30, 60, 120, 180 and 240 min) at constant and fixed N_2 flow rate of 450 sccm and NHP mass of 200 mg. Using NPN-2/NPNNS as a reference sample. Regardless of the annealing time, the entire sample denoted as NPN-5 (30 min), NPN-6 (60 min), NPN-7 (120 min) and NPN-8 (240 min) exhibited the same phases of Ni_5P_4 (Figure S9) indicating that the annealing time has less or no effect on the sample phase. Likewise, the TEM images of all the samples are characterized with homogeneous coated layer of $Ni^{2+\delta}O_\delta(OH)_{2-\delta}$ (Figure S10). However, according to HRTEM images derived from the corresponding TEM images in Figure S10, the thickness of the coated layer varies with different annealing time as depicted in Fig. 3. Starting from the precursor, its nanosheet consists of a smooth surface (Fig. 3a). With the reference sample NPN-2 thickness layer at 3 nm (Fig. 1c/3e), the thickness of the coated layer increases with increasing annealing time i.e. from 0.5 nm for NPN-5 (Fig. 3b) to 1 nm for NPN-6 (Fig. 3c), 2 nm for NPN-7 (Fig. 3d) and 4.5 nm for NPN-8 (Fig. 3f). Lattice fringes measured from each HRTEM images correspond to the hexagonal Ni_5P_4 phase (PDF#18-0883). We concluded that: (i) the amorphous $Ni^{2+\delta}O_\delta(OH)_{2-\delta}$ coated layer is annealing time dependent, annealing
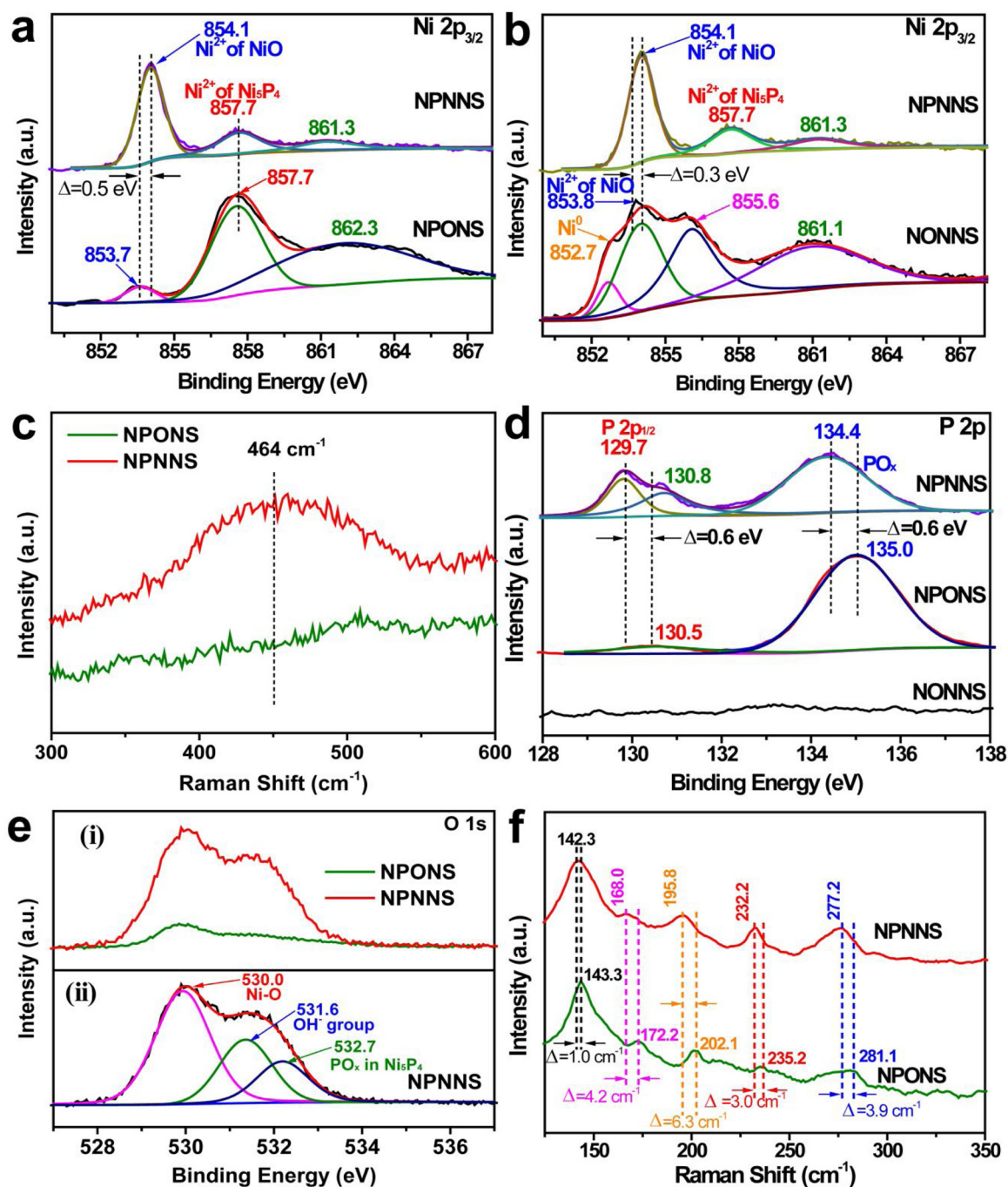
Fig. 2. Ni 2p XPS spectra of (a) NPONS and NPNNS and (b) NONNS and NPNNS. (c) Raman spectra of NPONS and NPNNS showing the Ni-OH band of NPNNS between 300 and 600 cm^{-1}. (d) P 2p XPS spectra of NPONS and NPNNS. (e) O 1s XPS spectra of NPONS and NPNNS. (f) Raman spectra of NPONS and NPNNS between 100 and 350 cm^{-1}.

gas flow rate reliant and phosphorus-source mass susceptible and (ii) our synthetic approach is a tunable approach to develop different Ni-P phases and hybrids with controllable thickness. It should be noted that the product of annealing Ni(OH)$_2$·0.75H$_2$O in N$_2$ in the absence of NHP is NiO-Ni hybrid nanosheets (denoted NONNS) with no coated layer (Figure S11).

3.4. HER properties in alkaline media

The HER electrocatalytic performance of the samples was first examined in 1.0 M KOH as electrolyte (Table S4) using a three-electrode configuration with a carbon rod counter electrode, a Ag/AgCl reference electrode, and the as-prepared samples as the working electrodes. Commercial Pt/C-CC was also employed for comparison. In 1.0 M KOH alkaline electrolyte, the catalytic performance of NPN-2/NPNNS hybrid outperformed the other controlled samples (Figures S12–S14). Thus, we compared the performance of NPONS, NPNNS, NONNS and Pt/C-CC electrocatalysts in 1.0 M KOH. The onset overpotential, overpotential at 10 mA cm^{-2} and Tafel slope of NPNNS catalyst are 33 mV, 87 mV and 69 mV dec^{-1}, respectively (Fig. 4a and b). These values are better than some other recently reported Ni-P-based catalysts [12,20,21,59,61–63], significantly lower than those of NPONS (88 mV, 157 mV and 90 mV dec^{-1}) and NONNS (99 mV, 203 mV and 164 mV dec^{-1}) and slightly inferior to that of Pt/C-CC (11 mV, 68 mV and 62 mV dec^{-1}),
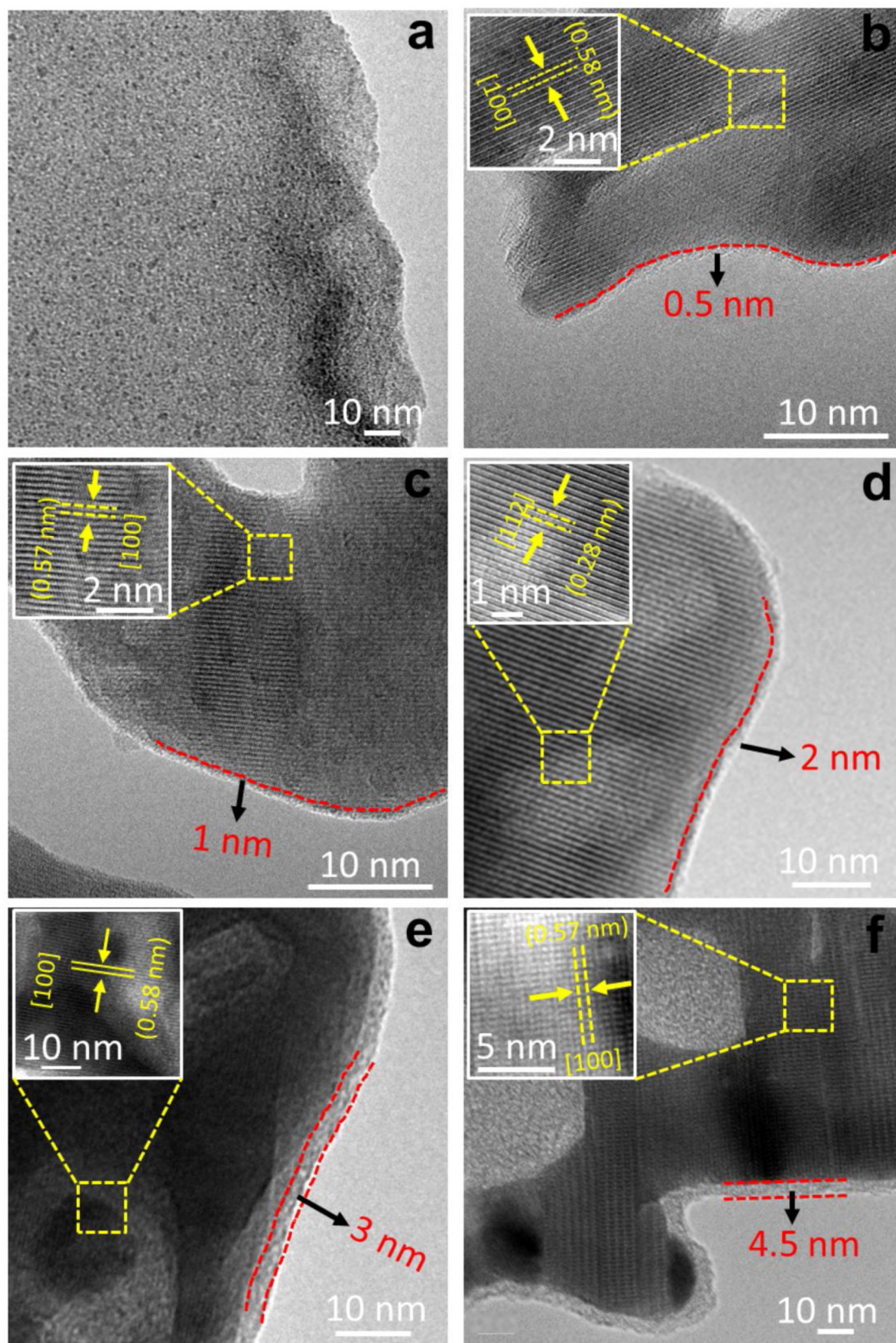
Fig. 3. Morphological characterization. (a) HRTEM image of Ni precursor. HRTEM images of the NPNNS annealed at desired duration of (b) NPN-5 (30 min), (c) NPN-6 (60 min), (d) NPN-7 (120 min), (e) NPN-2/NPNNS (180 min) and (f) NPN-8 (240 min) with their coated amorphous NiO layer values in nm. Inset in each image is the corresponding lattice fringes value derived from the HRTEM images.
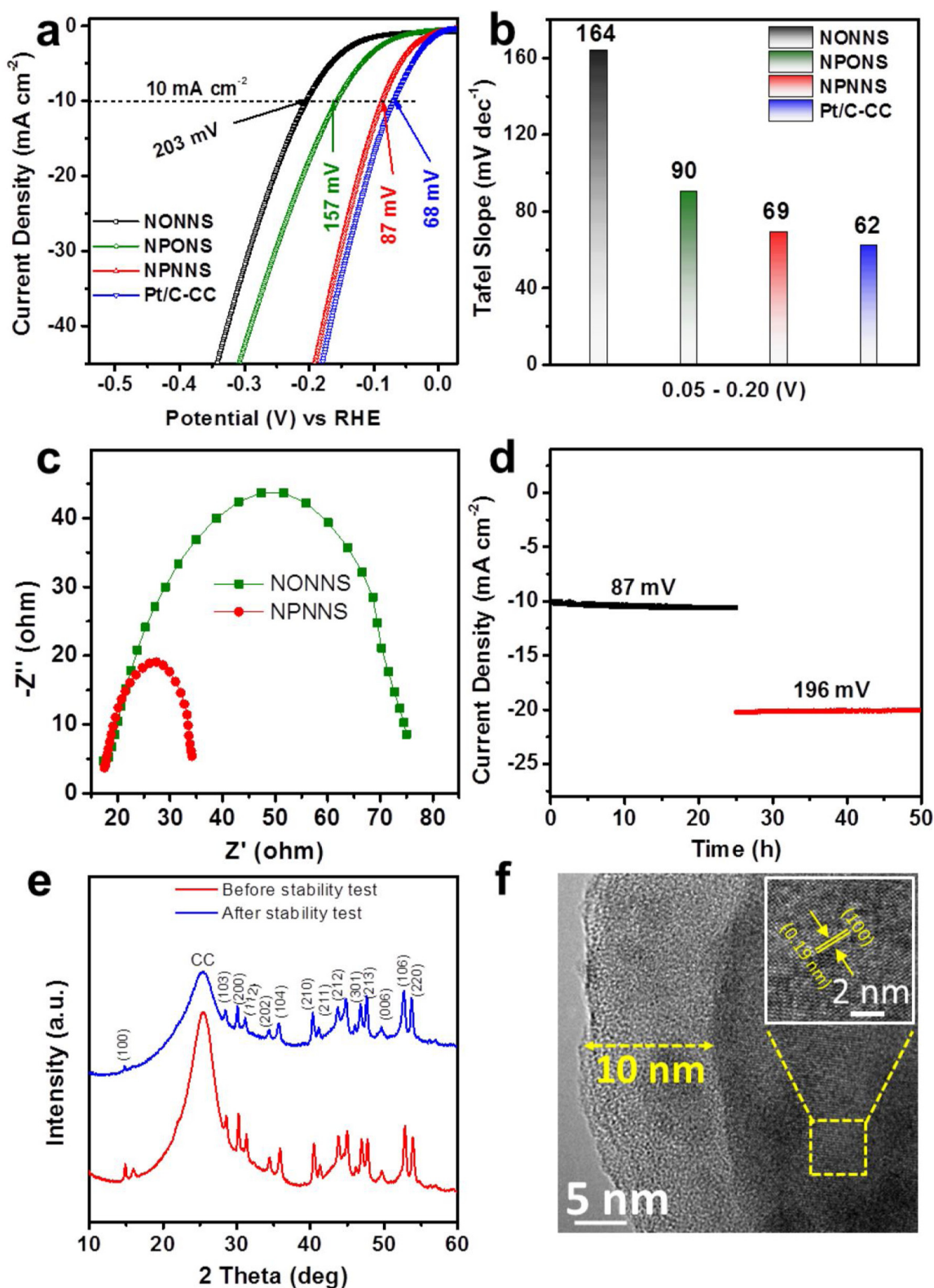
Fig. 4. HER properties in alkaline media. (a) Polarization curves and (b) Tafel slope of NONNS, NPONS, NPNNS and Pt/C-CC at a scan rate of 10 mV s^{-1} in 1.0 M KOH electrolyte. (c) Nyquist plot of NPONS and NPNNS electrocatalysts. (d) Stability test of NPNNS electrocatalyst at different overpotential in alkaline medium for 50 h. (e) XRD spectra of NPNNS before and after stability test in alkaline medium. (f) HRTEM image of NPNNS catalyst after CP stability measurement. Inset is the corresponding lattice fringes value.

respectively.

To investigate the electrode kinetics during HER process, the electrochemical impedance spectroscopy (EIS) measurements were

performed from 100 MHz to 0.01 Hz at overpotential of 100 mV (Fig. 4c). The semicircles in the Nyquist plot are related to the charge-transfer resistance (R_{ct}). Warburg impedance is absent in both catalysts,

indicating that transportation of mass is fast enough and the reaction is kinetically controlled [64]. The R_{ct} value of the NPNNS (35 Ω) is lower than that of NPONS (79 Ω), which is indicative of rapid reaction kinetics in the NPNNS. The results also correlate with the Tafel results. A video showing the hydrogen evolution by NPNNS can be seen in Supplemental Video SV1 (Figure S15). The capacitance of the catalysts (C_{dl}) was calculated based on the current density value at potential of 0.4 V vs. RHE at different scan rates and C_{dl} of NPNNS catalyst is 40.5 mF cm^{-2}, which is also higher than that of NONNS (27.2 mF cm^{-2}) (Figure S16a) further confirming that NPNNS is more electroactive than NPONS.

The durability test for NPNNS catalyst was performed via chronoamperometric measurements at different overpotentials for 50 h at two different overpotentials of 87 and 196 mV, which are equivalent to 10 and 20 mA cm^{-2}, respectively (Fig. 4d). After stability test, polarization curves of NPNNS electrocatalyst are identical (Figure S16b). XRD pattern of NPNNS catalyst after reaction is very similar to the unreacted one (Fig. 4e) suggesting excellent phase stability. Enlarge SEM images shows that the diameter of the nanosheets increases from about 50 nm (before reaction) to 90–100 nm (Figure S16c). This suggests that the nanosheets surface layer has exhibited some post-modification. According to TEM image, the surface of the nanosheet consists of thicker layer compared to the initial 3 nm layer (Fig. 4f). The reason for increment in the thickness of the amorphous shell is common to most other nickel phosphides after catalytic reaction. Previous reports have attributed the coated layer after electrolysis with hydroxides of corresponding metal compounds [39,65] such as NiOOH for Ni phosphides [20,59]. Similar situation was also observed in our case. For example, the HRTEM image collected from the TEM image shows that the coated amorphous layer of NPNNS sample has increased from 3 nm (before electrolysis) to 10 nm after electrolytic process. Lattice fringes of 0.19 nm can be identified for (100) line of the hexagonal Ni$_5$P$_4$ (Fig. 4f inset). Furthermore, two peaks at 423 cm^{-1} and 520 cm^{-1} were detected by the Raman spectra, which can be attributed to Ni-OH bending and stretching modes (Figure S16d), which suggest the presence of Ni oxide species and also indicates that the NPNNS surface layer is NiO/OH rich. Addtionally, Figure S16e and S16f shows that all the XPS peaks related to Ni^{2+} of both Ni$_5$P$_4$ core, Ni$^{2+\delta}$O$_8$(OH)$_{2-\delta}$ layer and P 2p of NPNNS hybrid showed no clear changes after HER process, indicating excellent stability of NPNNS in KOH. It should be pointed out that NPONS catalyst loses its catalytic performance (Figure S17).

3.5. HER properties in seawater media

A good electrocatalyst should also exhibit excellent performance in neutral medium as the traditional Pt-based catalysts show excellent electrocatalytic performances in wide pH-ranges [66,67]. With the development of Ni-P electrocatalysts for the HER in neutral media (e.g., phosphate-buffered solution, PBS) [59,66,67], the performance of Ni$_5$P$_4$ are less reported in neutral media [68]. Till date, there is no literature on Ni-P-based electrocatalysts for other neutral electrolyte such as seawater, and only one study on other TMP-based catalysts has been reported [69]. Splitting of H$_2$ from real seawater will create an opportunity for the massive production of hydrogen [8]. Therefore, Ni-P-based electrocatalysts that can function efficiently in acidic, alkaline and neutral (especially real seawater) media are highly important.

Firstly, the relative electrochemical active surface area (ECSA) of the electrocatalysts were determined by the capacitance of the double layer (C_{dl}) using cyclic voltammetry (CV) measurements in the potential region between 0.2–0.6 V vs. RHE in neutral real seawater electrolyte (pH = 7.8). The CV curves of NPONS and NPNNS are shown in Figures S18a and S18b, respectively. The capacitance of the catalysts was calculated based on the current density value at a potential of 0.4 V vs. RHE at each scan rate. According to Fig. 5a, the C_{dl} of the NPNNS catalyst is 28.2 mF cm^{-2}, which is double that of NPONS

(12.2 mF cm^{-2}), indicating that the ECSA of NPNNS is larger than that of NPONS. The HER catalytic properties of NPONS, NPNNS, NONNS and the Pt/C-CC were studied in real seawater electrolyte. According to the polarization curves in Fig. 5b, NPNNS showed a superior performance to that of NPONS and NONNS counterparts and also characterized by a low resistance (Figure S19), which indicated its excellent kinetics. At current density of 10 mA cm^{-2}, the overpotential NPNNS is of 144 mV and that of Pt is 121 mV. Interestingly, NPNNS exhibited Tafel slope of 108 mV dec^{-1}, which is significantly lower than that of Pt/C-CC (156 mV dec^{-1}) (Fig. 5c). NPNNS also displayed attractive H$_2$ evolution in a video demonstration (Supplemental Video SV2 and Figure S20), which showed the potential application of NPNNS as efficient catalyst for H$_2$ evolution from real seawater. It has been previously reported that the HER mechanism should exhibit the Volmer-Tafel or Volmer-Heyrovsky process, regardless of the pH conditions [1]. Thus, the Tafel slope of NPNNS is very close to 120 mV dec^{-1} (Volmer-Heyrovsky pathway) [1,70,71], which showed that the catalyst exhibited a Volmer-Heyrovsky reaction mechanism. The Volmer-Heyrovsky mechanism is displayed below [8]:

$$H_2O + e^- \rightarrow H_{ads} + OH^- (Volmer) \tag{4}$$

$$H_{ads} + H_2O + e^- \rightarrow H_2 + OH^- (Heyrovsky) \tag{5}$$
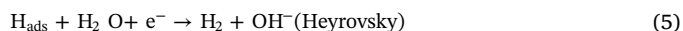
NPNNS displayed a comparable onset potential and overpotential to that of other reported electrocatalysts [69,72,73] and a Tafel slope superior to that of most reported electrocatalysts for seawater splitting [8,69,72–76] (See details comparison in Table 1).

The amount of H$_2$ gas evolved during evolution, analysis of the products and faradaic efficiency are very crucial. To confirm the effectiveness of NPNNS catalyst, the amount of H$_2$ gas within 3600 s of electrolysis (using the chronoamperometric *i-t* curve) in a 40 mL real seawater was determined using in situ gas chromatography for the NPONS, NPNNS and Pt/C-CC electrocatalysts (Fig. 5d). The faradaic efficiency was 93% (Figure S21), which suggested little or no other multi-reactions occurred during the electrolysis. The NPNNS catalyst evolved 7 μmol, 15 μmol and 22 μmol of hydrogen gas at 1200 s, 2400 s and 3600 s, respectively, displaying a uniform and linear increment, which suggested a better stability than that of NPONS. Although, Pt/C-CC evolved larger amount of H$_2$ gas than NPNNS but the amount decreased over time indicating that the Pt had poor stability. These results further confirmed the potential application of NPNNS as an efficient electrocatalyst for H$_2$ evolution in real seawater.

The optimal NPNNS hybrid also achieved superb chronopotentiometric measurement stability at various current densities of 10, 30, 50 and 100 mA cm^{-2} for 40 h (Fig. 5e). After the durability test, NPNNS could still maintain its initial onset potential and overpotentials (Figure S22a), showed attractive phase and morphological stability (Figure S22b and S22c). Furthermore, XPS analyses of NPNNS hybrid after stability test shows all the electronic states of Ni and P can be maintained (Figure S23). To confirm that the amorphous layer of NPNNS hybrid is stable in real seawater electrolyte during HER, EDS analysis of NPNNS after stability test were studied. The EDS mapping displayed in Fig. 5f confirms the uniform distribution of Ni and P in the core district and that the shell is mainly an O layer, which is also in accordance with results obtained before H$_2$ evolution. However, NPONS electrocatalyst did not retain its initial catalytic properties after the stability test due to morphological damage (Figure S24). The excellent performance of NPNNS hybrid is due to the synergistic effect between Ni$_5$P$_4$ and Ni$^{2+\delta}$O$_8$(OH)$_{2-\delta}$ that allows easy adsorption on H and OH and hence facilitating rapid water dissociation and the entire HER process.

3.6. HER properties in acidic media

The polarization curves of NONNS, NPONS, NPNNS and Pt/C-CC in 0.5 M H$_2$SO$_4$ (acidic medium) can be seen in Fig. 6a. Interestingly, the onset overpotential and overpotential at 10 mA cm^{-2} of NPNNS is
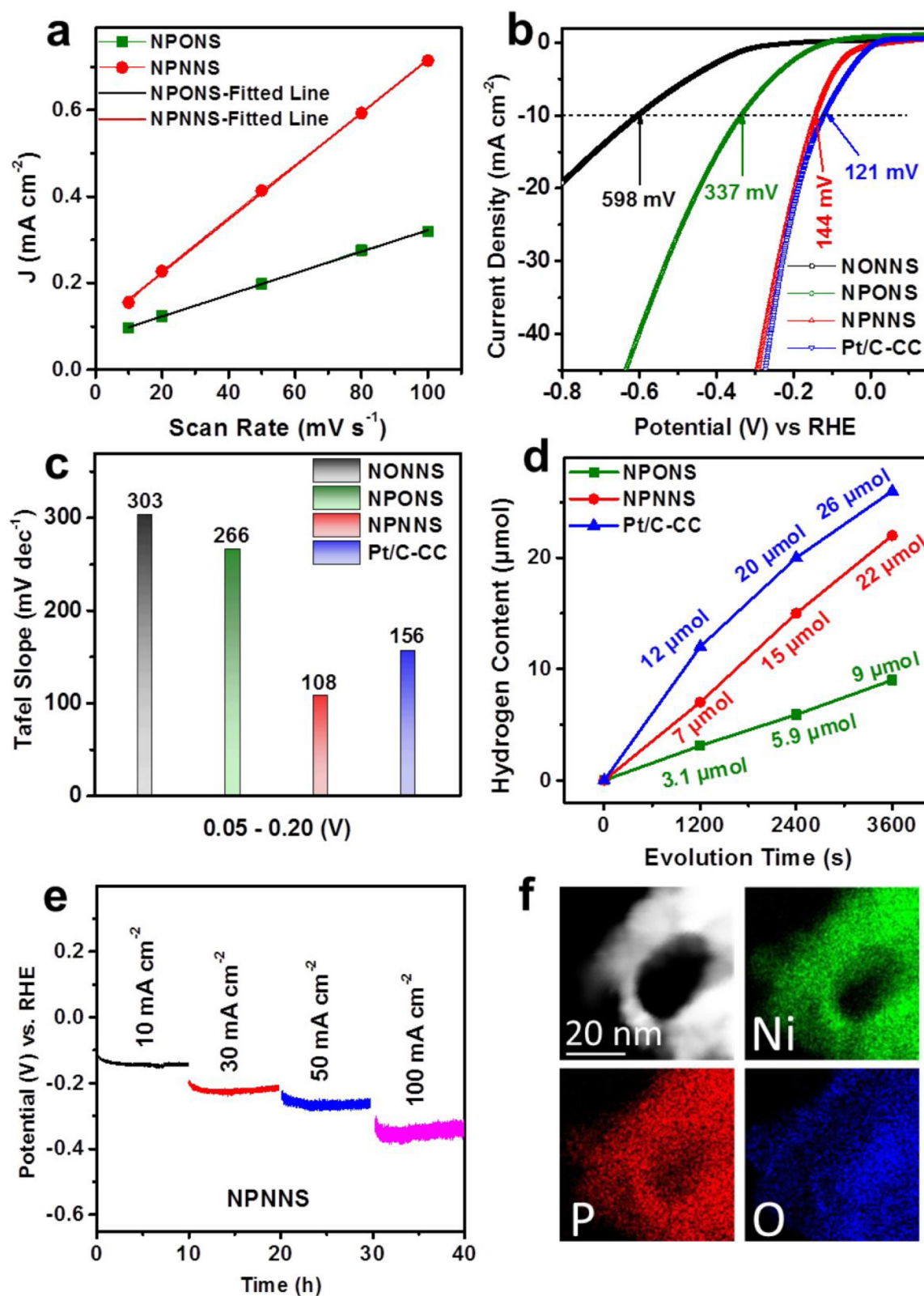
Fig. 5. HER properties in real seawater (neutral) media. (a) Scan rate dependence of the current density at potential of 0.4 V vs. RHE for NPONS and NPNNS electrocatalysts in real seawater electrolyte. (b) Polarization curves and (c) Tafel slope of NONNS, NPONS, NPNNS and Pt/C-CC at a scan rate of 10 mV s^{-1} in real seawater (neutral) electrolyte (pH = 7.8). (d) Comparison of the amount of hydrogen gas evolved by the catalysts at overpotential of 130 mV for 3600 s. (e) CP stability measurements of NPNNS catalyst at current densities of 10, 30, 50 and 100 mA cm^{-2} in real seawater electrolyte. (f) EDS elemental mapping of the NPNNS catalyst after the stability test.

Table 1

HER performances of NPNNS and other reported electrocatalysts in the seawater splitting.

Electrocatalysts	Onset potential (mV)	Overpotential (mV) @10 mA cm^{-2}	Tafel slope
NPNNS (this work)	**90**	**144**	**108**
NPNNS (this work)	132	337	266
NONNS (this work)	312	598	303
Pt/C-CC	38	266	216
RuCo [74]	250	~300	107
Cobalt-Sulfide [78]	43	~200	93
Pt–Ru–Cr [73]	130	286	126
Pt–Ru–Fe [73]	126	248	122
Pt–Ru–Co [73]	113	222	110
Pt–Ru–Ni [73]	103	206	104
Pt–Ru–Mo [73]	96	196	100
Nickel foam [75]	400	695	262
Co$_3$Mo$_3$C/CNT [75]	42	124	249
Commercial CNT [75]	400	600	–
Co,N-doped nanocarbons [76]	83	240	159
Mn-NiO-Ni/Ni-F [8]	90	170	–

10 mV and 66 mV, respectively, which is highly comparable to that of Pt/C-CC (6 mV and 54 mV) and better those of NONNS (316 mV and 481 mV) and NPONS (48 mV and 121 mV). These NPNNS values are superior to some of the recently reported Ni$_5$P$_4$ electrocatalysts [20,63]. As the current density of NPNNS increased to 40 mA cm^{-2}, the NPNNS catalyst delivered a lower overpotential than the Pt/C-CC, which suggested that NPNNS is also promising in achieving a low potential at higher current densities. The rate-determining step (RDS) of HER reaction is either a discharge reaction (Volmer step) followed by combination reaction (Volmer-Tafel step) or followed by desorption reaction (Volmer-Heyrovsky process) [70]. The Tafel slope of the discharge reaction is theoretically equivalent to 29 mV dec^{-1} (2.3$RT/2F$). Hence, the Tafel slope of NPNNS (33 mV dec^{-1}) is higher than those of NPONS (74 mV dec^{-1}) and NONNS (176 mV dec^{-1}) but almost the same with that of Pt/C-CC (31 mV dec^{-1}) (Fig. 6b) indicating that NPNNS hybrid exhibits a Pt-like HER mechanism with Tafel reaction as the RDS. The superior kinetics of NPNNS hybrid during the HER process is made more clear by the electrochemical impedance spectroscopy (EIS) (Fig. 6c). The semicircles in the Nyquist plots are related to the charge-transfer resistance (R_{ct}) and the lower the R_{ct} value, the better the kinetics and conductivity of a material [64]. Thus, the R_{ct} value of NPNNS (34 Ω) is obviously lower than that of NPONS (42 Ω), further justifying rapid reaction kinetics and enhanced conductivity in NPNNS hybrid. Both Tafel and Nyquist plots suggest faster HER catalytic pathways and
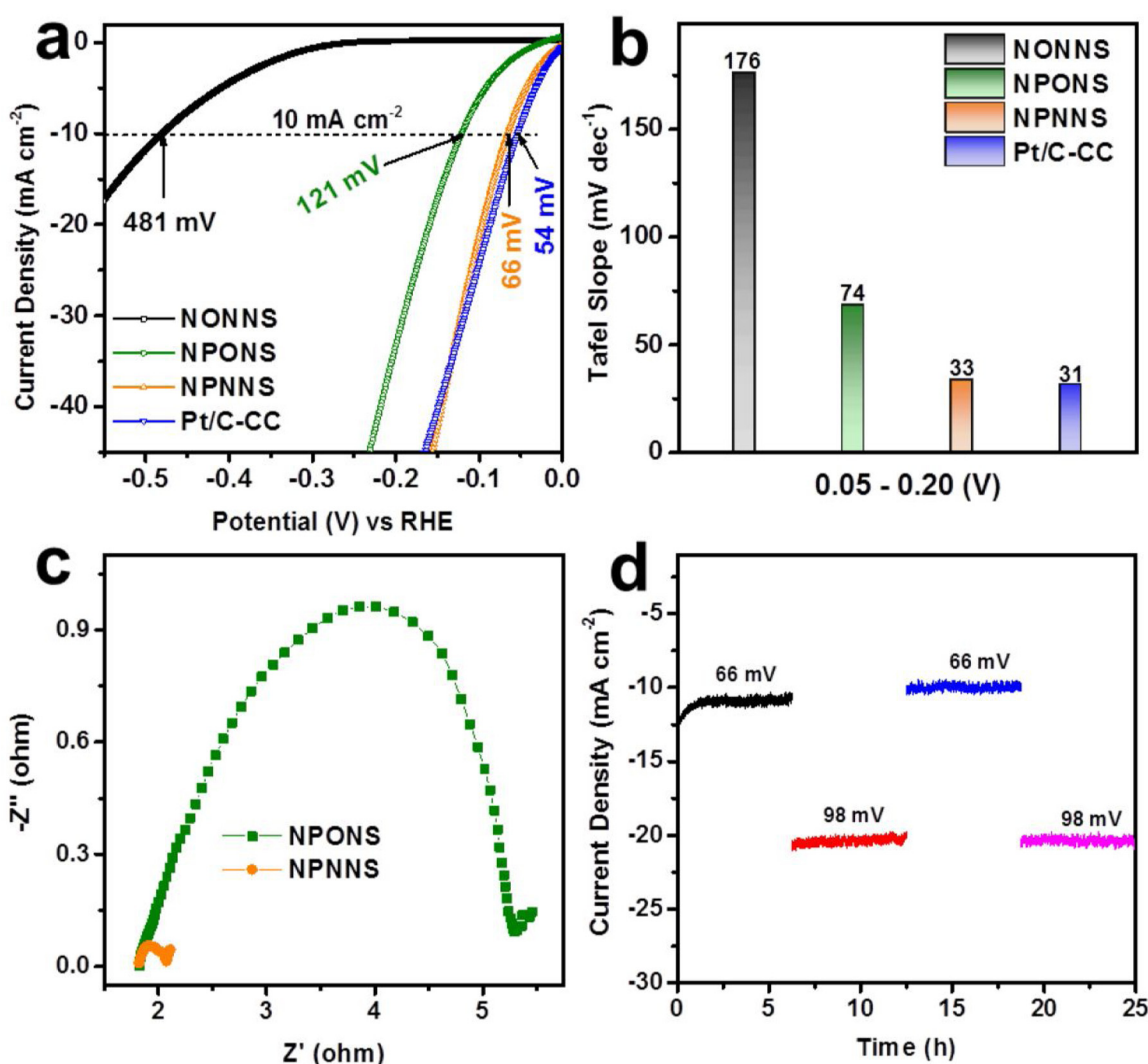

Fig. 6. HER properties in acidic media. (a) Polarization curves and (b) Tafel slope of NONNS, NPONS, NPNNS and Pt/C-CC at a scan rate of 10 mV s^{-1} in 0.5 M H$_2$SO$_4$ electrolyte. (c) Nyquist plot of NPONS and NPNNS electrocatalysts. (d) Stability test of NPNNS electrocatalyst at different overpotential in acidic medium for 25 h.

favorable kinetics on the NPNNS than those of NONNS and NPONS. Amperometric measurements were performed at various overpotentials of 66 mV and 98 mV corresponding to current densities of 10 and 20 mA cm^{-2} for NPNNS hybrid (Fig. 6d). The catalyst maintained excellent stability at these overpotentials after 25 h. The LSV curves after each CP measurements were identical, which confirmed the excellent stability of the NPNNS electrocatalyst (Figure S25a). Additionally, XRD pattern of NPNNS catalyst after stability test are very similar to that of the unreacted one (Figure S25b) suggesting excellent phase stability. SEM images show that the nanosheet morphology can be retained (Figure S25c). TEM images also confirmed the presence of the nano Ni$^{2+\delta}$O$_\delta$(OH)$_{2-\delta}$ layer (Figure S25d). Moreover, XPS analyses clarified that the elemental valence states can be identified which are nearly the same with the initial sample (Figure S25e and S25f). Hence, based on SEM, TEM, XRD and XPS results, we affirmed that the Ni$^{2+\delta}$O$_\delta$(OH)$_{2-\delta}$ layer could not be dissolved in acidic environment. To further confirm that the amorphous layer of NPNNS hybrid is stable in the acidic electrolyte during HER, inductively coupled plasma mass spectrometry (ICP) analyses of NPNNS after stability test is studied. Details can be found in Figure S26. However, NPONS displayed morphological damage owing to its poor stability after stability test (Figure S27).

4. Discussion

4.1. Suppressing the P-H bonds

As mentioned above, the hybridization of Ni$_5$P$_4$ with nickel hydr (oxyl)oxide is to suppress the P-H$_{ads}$ bonds in order to promote water adsorption and activation for HER. Thus, Raman spectra were employed to study the bonding states of P-H$_{ads}$ intermediate on NPONS and NPNNS after HER in all electrolytes as shown in Fig. 7. A Raman peak at 1065 cm^{-1} that is attributed to the P-H$_{ads}$ bonds [77] is observed in NPNNS and NPONS in Fig. 7a–c. The P-H$_{ads}$ bonds of NPNNS show lower intensity than that of NPONS and absent in the electrolytes in the alkaline media (Fig. 7a), real seawater media (Fig. 7b) and acidic media (Fig. 7c). This is indicative of weaker P-H$_{ads}$ bonds that are beneficial for convenient generation of H on the NPNNS catalyst surface than the NPONS during HER. Additionally, the peak assigned to the bending vibrations of O-H bonds of adsorbed H$_2$O on the surfaces of catalysts can be located at ~1643 cm^{-1}. As can be seen in Fig. 7a–c, the intensity of O-H bending vibration in NPNNS is stronger than that of NPONS and all the electrolytes. Furthermore, the peaks exhibit a Raman shift to the lower wavelength compared to those of NPONS and the electrolytes as well. Such results indicate that the O-H bonds of adsorbed water on NPNNS are weaker than those on NPONS and the electrolytes. Hence, the electronic interactions between Ni$_5$P$_4$ and Ni$^{2+\delta}$O$_\delta$(OH)$_{2-\delta}$ of NPNNS could not only depressed P-H$_{ads}$ bonds formed on catalyst surfaces to optimize H desorption in promoting HER

catalytic pathway but also promote water activation and adsorption for enhanced HER performance.

4.2. NBO charge distribution

Electronic interaction between two samples has been proven to both promote the H adsorption for H$_{ads}$ formation and enhance Tafel step for efficient H$_{ads}$ transfer [78]. As a result of the electronic interactions, the NBO charge redistribution of the Ni of NPONS, Ni of NPNNS and Ni$^{2+\delta}$O$_\delta$(OH)$_{2-\delta}$, Ni of Ni$^{2+\delta}$O$_\delta$(OH)$_{2-\delta}$, P of NPONS, P of NPNNS, O of NPNNS and O of Ni$^{2+\delta}$O$_\delta$(OH)$_{2-\delta}$ were derived from the density functional theory (DFT) calculations as shown in Fig. 8a. For the DFT calculations, the optimized structures and cluster models of NPONS, NPNNS and Ni$^{2+\delta}$O$_\delta$(OH)$_{2-\delta}$ are shown in Figure S28. In NPNNS, the Ni of Ni$_5$P$_4$ and Ni$^{2+\delta}$O$_\delta$(OH)$_{2-\delta}$ carry more positive charges and the P of NPNNS carry less negative charges compared with NPONS and Ni$^{2+\delta}$O$_\delta$(OH)$_{2-\delta}$. This result implies that electronic interaction took place between the P of Ni$_5$P$_4$ increases and the Ni of Ni$^{2+\delta}$O$_\delta$(OH)$_{2-\delta}$. This is in good agreement with the results and conclusion obtained from our XPS results that the Ni of Ni$^{2+\delta}$O$_\delta$(OH)$_{2-\delta}$ exhibited positive binding energy shift while P of Ni$_5$P$_4$ exhibited negative binding energy shift (Fig. 2).

4.3. Water and hydrogen adsorption activity

Furthermore, based on the fact that water molecules consist of two positively charged H atoms and one negatively charged O atom, the charge redistribution of NPNNS allows the positively charged Ni of the hybrid for adsorption and activation of H$_2$O molecules by securing the O and OH atoms of H$_2$O. Thus, the water adsorption free energies on various catalysts studied by DFT calculations from the electrocatalysts optimized structures and cluster models (Figure S29) show that the NPNNS owns the lowest water adsorption energy, suggesting that water absorption on NPNNS is easier than those on NPONS and Ni$^{2+\delta}$O$_\delta$(OH)$_{2-\delta}$ (Fig. 8b). Those results above suggest that the surface of NPNNS is more beneficial for water adsorption, thus the HER will be more beneficial compared with those of NPONS and Ni$^{2+\delta}$O$_\delta$(OH)$_{2-\delta}$.

The electronic interactions between Ni$^{2+\delta}$O$_\delta$(OH)$_{2-\delta}$ and Ni$_5$P$_4$ of NPNNS have been experimentally proven to weaken the P-H$_{ads}$ bonds formed on catalyst surfaces in order to optimize H adsorption. Hence, Fig. 8c sheds more light on the theoretical results. During HER, the H atoms will increase on the P$_3$-hollow site and more P-H$_{ads}$ bonds were formed, which could negatively affect H adsorption [23]. At first, the DFT calculations have proven that the H adsorption on NPONS is too strong and that of NONNS is stronger, leading to low HER electrocatalytic properties of both catalysts. Compared with individual Ni$^{2+\delta}$O$_\delta$(OH)$_{2-\delta}$ and NPONS, the optimal Gibbs free energy change for catalyst-H* (ΔGH*) value of NPNNS determined from the optimized H
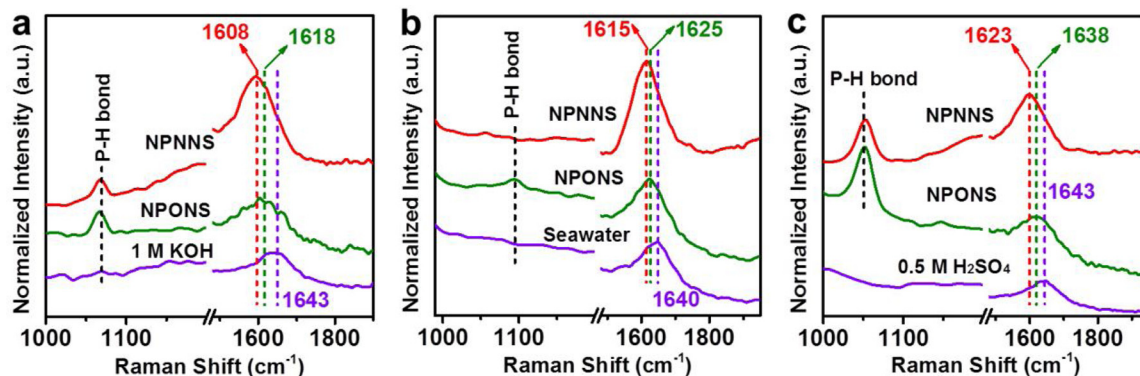

Fig. 7. Raman spectra of the electrolyte, NPONS and NPNNS in (a) 1.0 M KOH, (b) real seawater and (c) 0.5 M H$_2$SO$_4$ showing the weakening of the P-H$_{ads}$ bonds and water adsorption properties of the electrocatalysts.
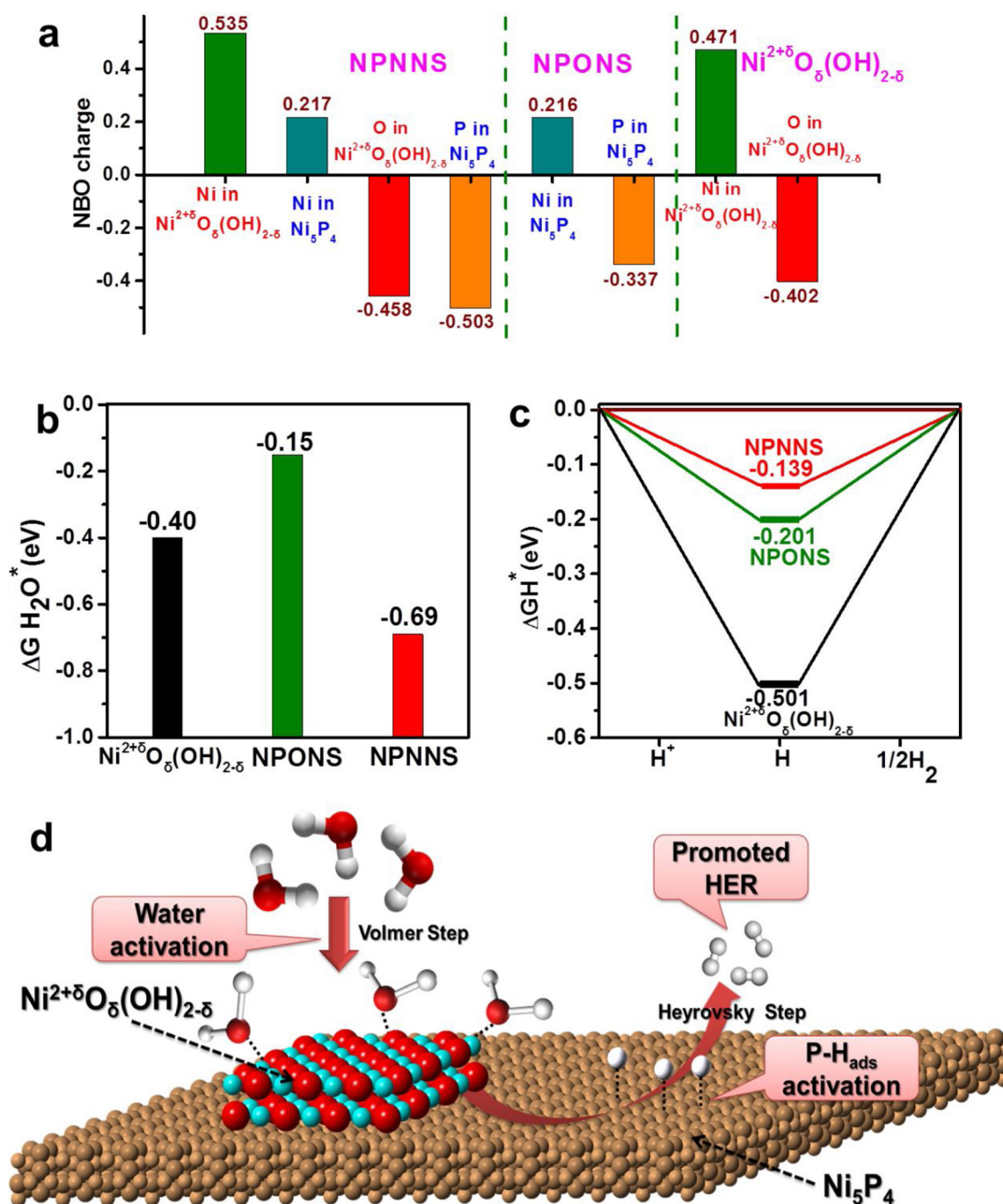
Fig. 8. (a) Charge density distributions of $Ni^{2+\delta}O_\delta(OH)_{2-\delta}$, NPONS and NPNNS. (b) Calculated adsorption free energy changes of H_2O on $Ni^{2+\delta}O_\delta(OH)_{2-\delta}$, NPONS and NPNNS. (c) Calculated free-energy diagram of HER for $Ni^{2+\delta}O_\delta(OH)_{2-\delta}$, NPONS and NPNNS. (d) Schematic mechanism of water adsorption, water activation, and hydrogen generation processes by NPNNS electrocatalyst.

of the electrocatalysts (Figure S30) is quite close to 0 eV [27,50], and this value will lead to the ideal H adsorption on the surface of catalyst and accordingly will benefit rapid catalytic step of HER (Fig. 8c). This indicates that the P-H_{ads} bonds on NPNNS are very appropriate and also in accordance with the experimental results obtained in Figs. 4 and 5, hence, resulting in higher HER activities for the NPNNS. For the above discussions, Fig. 7d schematically revealed the mechanism of operation of NPNNS hybrid, where Ni_5P_4 serve as acceptor of H and the amorphous $Ni^{2+\delta}O_\delta(OH)_{2-\delta}$ virtually adsorb H_2O molecules, which is useful for H-O cleavage for enhanced water dissociation and triggering both Volmer and Heyrovsky kinetic pathways.

5. Conclusions

In conclusion, we have successfully developed a facile approach to design $Ni_5P_4@Ni^{2+\delta}O_\delta(OH)_{2-\delta}$ hybrid nanosheets (NPNNS) as efficient electrocatalyst for the production of hydrogen in acidic, alkaline and neutral media. The hybrid electrocatalyst was produced by the treatment of hydrothermally derived $Ni(OH)_2 \cdot 0.75H_2O$ precursor in N_2 gas and $NaH_2PO_2 \cdot H_2O$, and $Ni^{2+\delta}O_\delta(OH)_{2-\delta}$ amorphous nanolayer can be controlled by tuning the phosphorus-source content, annealing scan rate and duration. The resultant, $Ni_5P_4@Ni^{2+\delta}O_\delta(OH)_{2-\delta}$ hybrid (NPNNS) exhibit superior catalytic performance (such as a low onset overpotential, small Tafel slope and low charge-transfer resistance) and

durability over the pristine Ni$_5$P$_4$ nanosheets (NPONS) and phosphorus-free NiO-Ni (NONNS) as electrocatalyst for HER in alkaline, seawater and acidic electrolytes. Both theoretical and experimental analyses reveal that the electronic interactions and synergistic effect between Ni$_5$P$_4$ and Ni$^{2+\delta}$O$_8$(OH)$_{2-\delta}$ is not only favorable for weakening the P-H$_{ads}$ bonds and fasten H$_2$O activation and adsorption but Ni$^{2+\delta}$O$_8$(OH)$_{2-\delta}$ could also useful as protective layer. Such interactions optimize the H adsorption and desorption on the Ni-P surface and efficiently enhance HER catalytic pathways. Both "metal-metal interaction" and "hybridization" theories indicate the electronic interaction between nickel hydr(oxy)oxide and metallic nature of Ni$_5$P$_4$. This present work sheds more light on new approach to promote the electrocatalytic activity of TMPs through weakening the strong P-H$_{ads}$ bonds by nanohybridization and also creates opportunity for the potential utilization of TMPs for hydrogen evolution at wide pH range especially in abundant real seawater.

Acknowledgments

Appendix A. Supplementary data

Supplementary data associated with this article can be found, in the online version, at https://doi.org/10.1016/j.apcatb.2019.03.037.

References

[1] Y. Shi, B. Zhang, Chem. Soc. Rev. 45 (2016) 1529–1541.
[2] Z.W. Seh, J. Kibsgaard, C.F. Dickens, I. Chorkendorff, J.K. Nørskov, T.F. Jaramillo, Science 355 (2017).
[3] G. Li, Y. Sun, J. Rao, J. Wu, A. Kumar, Q.N. Xu, C. Fu, E. Liu, G.R. Blake, P. Werner, B. Shao, K. Liu, S. Parkin, X. Liu, M. Fahlman, S.-C. Liou, G. Auffermann, J. Zhang, C. Felser, X. Feng, Adv. Energy Mater. 8 (2018) 1801258.
[4] M. Ledendecker, H. Schlott, M. Antonietti, B. Meyer, M. Shalom, Adv. Energy Mater. 7 (2017) 1601735.
[5] Q. Ding, B. Song, P. Xu, S. Jin, Chemistry 1 (2016) 699–726.
[6] S. Gupta, N. Patel, R. Fernandes, R. Kadrekar, A. Dashora, A.K. Yadav, D. Bhattacharyya, S.N. Jha, A. Miotello, D.C. Kothari, Appl. Catal. B-Environ. 192 (2016) 126–133.
[7] R. Ma, E. Song, Y. Zhou, Z. Zhou, G. Liu, Q. Liu, J. Liu, Y. Zhu, J. Wang, Energy Stor. Mater. 6 (2017) 104–111.
[8] X. Lu, J. Pan, E. Lovell, T.H. Tan, Y.H. Ng, R. Amal, Energy Environ. Sci. 11 (2018) 1898–1910.
[9] H. Yan, C. Tian, L. Wang, A. Wu, M. Meng, L. Zhao, H. Fu, Angew. Chem. Int. Ed. 54 (2015) 6325–6329.
[10] C. Ouyang, X. Wang, S. Wang, Chem. Commun. 51 (2015) 14160–14163.
[11] Z. Pu, S. Wei, Z. Chen, S. Mu, Appl. Catal. B-Environ. 196 (2016) 193–198.
[12] A.-L. Wang, J. Lin, H. Xu, Y.-X. Tong, G.-R. Li, J. Mater. Chem. A 4 (2016) 16992–16999.
[13] E.J. Popczun, J.R. McKone, C.G. Read, A.J. Biacchi, A.M. Wiltrout, N.S. Lewis, R.E. Schaak, J. Am. Chem. Soc. 135 (2013) 9267–9270.
[14] J.F. Callejas, C.G. Read, C.W. Roske, N.S. Lewis, R.E. Schaak, Chem. Mater. 28 (2016) 6017–6044.
[15] Y. Zhang, L. Gao, E.J.M. Hensen, J.P. Hofmann, ACS Energy Lett. 3 (2018) 1360–1365.
[16] Z.-Z. Luo, Y. Zhang, C. Zhang, H.T. Tan, Z. Li, A. Abutaha, X.-L. Wu, Q. Xiong, K.A. Khor, K. Hippalgaonkar, J. Xu, H.H. Hng, Q. Yan, Adv. Energy Mater. 7 (2017) 1601285.
[17] C. Huang, T. Ouyang, Y. Zou, N. Li, Z.-Q. Liu, J. Mater. Chem. A 6 (2018) 7420–7427.
[18] H. Huang, C. Yu, C. Zhao, X. Han, J. Yang, Z. Liu, S. Li, M. Zhang, J. Qiu, Nano Energy 34 (2017) 472–480.
[19] A.B. Laursen, K.R. Patraju, M.J. Whitaker, M. Retuerto, T. Sarkar, N. Yao, K.V. Ramanujachary, M. Greenblatt, G.C. Dismukes, Energy Environ. Sci. 8 (2015)

[20] M. Ledendecker, S. Krick Calderón, C. Papp, H.P. Steinrück, M. Antonietti, M. Shalom, Angew. Chem. Int. Ed. 54 (2015) 12361.
[21] Y. Pan, Y. Liu, J. Zhao, K. Yang, J. Liang, D. Liu, W. Hu, D. Liu, Y. Liu, C. Liu, J. Mater. Chem. A 3 (2015) 1656–1665.
[22] M. Ledendecker, J.S. Mondschein, O. Kasian, S. Geiger, D. Göhl, M. Schalenbach, A. Zeradjanin, S. Cherevko, R.E. Schaak, K. Mayrhofer, Angew. Chem. Int. Ed. 56 (2017) 9767–9771.
[23] R.B. Wexler, J.M.P. Martirez, A.M. Rappe, ACS Catal. (2017) 7718–7725.
[24] P.W. Menezes, A. Indra, C. Das, C. Walter, C. Göbel, V. Gutkin, D. Schmeißer, M. Driess, ACS Catal. 7 (2017) 103–109.
[25] J.-X. Feng, S.-Y. Tong, Y.-X. Tong, G.-R. Li, J. Am. Chem. Soc. 140 (2018) 5118–5126.
[26] S.K. Kim, Y. Qiu, Y.-J. Zhang, R. Hurt, A. Peterson, Appl. Catal. B-Environ. 235 (2018) 36–44.
[27] J.-X. Feng, H. Xu, Y.-T. Dong, X.-F. Lu, Y.-X. Tong, G.-R. Li, Angew. Chem. Int. Ed. 56 (2017) 2960–2964.
[28] M.B. Gawande, A. Goswami, T. Asefa, H. Guo, A.V. Biradar, D.-L. Peng, R. Zboril, R.S. Varma, Chem. Soc. Rev. 44 (2015) 7540–7590.
[29] M. Gong, W. Zhou, M.-C. Tsai, J. Zhou, M. Guan, M.-C. Lin, B. Zhang, Y. Hu, D.-Y. Wang, J. Yang, S.J. Pennycook, B.-J. Hwang, H. Dai, Nat. Commun. 5 (2014) 4695.
[30] X. Li, W. Liu, M. Zhang, Y. Zhong, Z. Weng, Y. Mi, Y. Zhou, M. Li, J.J. Cha, Z. Tang, H. Jiang, X. Li, H. Wang, Nano Lett. 17 (2017) 2057–2063.
[31] P. Wang, K. Jiang, G. Wang, J. Yao, X. Huang, Angew. Chem. 55 (2016) 12859.
[32] Y. Yang, M. Luo, W. Zhang, Y. Sun, X. Chen, S. Guo, Chemistry 4 (2018) 2054–2083.
[33] Y. Hu, H. Yang, J. Chen, T. Xiong, M.S.J.T. Balogun, Y. Tong, ACS Appl. Mater. Interfaces 11 (2019) 5152–5158.
[34] Y. Huang, Y. Lu, Y. Lin, Y. Mao, G. Ouyang, H. Liu, S. Zhang, Y. Tong, J. Mater. Chem. A 6 (2018) 24740–24747.
[35] T. Ouyang, Y.-Q. Ye, C.-Y. Wu, K. Xiao, Z.-Q. Liu, Angew. Chem. Int. Ed. (2019), https://doi.org/10.1002/anie.201814262|.
[36] S. Dou, X. Wang, S. Wang, Small Methods 3 (2019) 1800211.
[37] X. Sun, J. Huo, Y. Yang, L. Xu, S. Wang, J. Energy Chem. 26 (2017) 1136–1139.
[38] C. Ouyang, S. Feng, J. Huo, S. Wang, Green Energy Environ. 2 (2017) 134–141.
[39] H. Zhang, X. Li, A. Hähnel, V. Naumann, C. Lin, S. Azimi, S.L. Schweizer, A.W. Maijenburg, R.B. Wehrspohn, Adv. Funct. Mater. 28 (2018) 1706847.
[40] J. Hu, C. Zhang, L. Jiang, H. Lin, Y. An, D. Zhou, M.K.H. Leung, S. Yang, Joule 1 (2017) 383–393.
[41] Q. Sun, N. Wang, Q. Bing, R. Si, J. Liu, R. Bai, P. Zhang, M. Jia, J. Yu, Chemistry 3 (2017) 477–493.
[42] X. Yu, J. Zhao, L.-R. Zheng, Y. Tong, M. Zhang, G. Xu, C. Li, J. Ma, G. Shi, ACS Energy Lett. 3 (2018) 237–244.
[43] L. Dang, H. Liang, J. Zhuo, B.K. Lamb, H. Sheng, Y. Yang, S. Jin, Chem. Mater. 30 (2018) 4321–4330.
[44] S. Baranton, C. Coutanceau, Appl. Catal. B-Environ. 136–137 (2013) 1–8.
[45] R. Liu, Y. Wang, D. Liu, Y. Zou, S. Wang, Adv. Mater. 29 (2017) 1701546.
[46] X. Zhang, Y. Liang, Adv. Sci. 5 (2018) 1700644.
[47] X. Yan, L. Tian, M. He, X. Chen, Nano Lett. 15 (2015) 6015–6021.
[48] A. Wu, C. Tian, H. Yan, Y. Jiao, Q. Yan, G. Yang, H. Fu, Nanoscale 8 (2016) 11052–11059.
[49] L. Lang, Y. Shi, J. Wang, F.-B. Wang, X.-H. Xia, ACS Appl. Mater. Interfaces 7 (2015) 9098–9102.
[50] J.-X. Feng, J.-Q. Wu, Y.-X. Tong, G.-R. Li, J. Am. Chem. Soc. 140 (2018) 610–617.
[51] M.-S. Balogun, W. Qiu, H. Yang, W. Fan, Y. Huang, P. Fang, G. Li, H. Ji, Y. Tong, Energy Environ. Sci. 9 (2016) 3411–3416.
[52] M.C. Biesinger, B.P. Payne, A.P. Grosvenor, L.W.M. Lau, A.R. Gerson, R.S.C. Smart, Appl. Surf. Sci. 257 (2011) 2717–2730.
[53] R. Subbaraman, D. Tripkovic, K.C. Chang, D. Strmcnik, A.P. Paulikas, P. Hirunsit, M. Chan, J. Greeley, V. Stamenkovic, N.M. Markovic, Nat. Mater. 11 (2012) 550.
[54] H.B. Li, M.H. Yu, F.X. Wang, P. Liu, Y. Liang, J. Xiao, C.X. Wang, Y.X. Tong, G.W. Yang, Nat. Commun. 4 (2013) 1894.
[55] Y. Gao, H. Li, G. Yang, Cryst. Growth Des. 15 (2015) 4475–4483.
[56] A.P. Grosvenor, M.C. Biesinger, R.S.C. Smart, N.S. Mcintyre, Surf. Sci. 600 (2006) 1771–1779.
[57] H. Xu, Y. Hu, D. Huang, Y. Lin, W. Zhao, Y. Huang, S. Zhang, Y. Tong, ACS Sustain. Chem. Eng. (2019), https://doi.org/10.1021/acssuschemeng.8b05336.
[58] X. Fan, M.-S. Balogun, Y. Huang, Y. Tong, ChemElectroChem 4 (2017) 2453–2459.
[59] S. Wang, L. Zhang, X. Li, C. Li, R. Zhang, Y. Zhang, H. Zhu, Nano Res. 10 (2017) 415–425.
[60] J. Zheng, W. Zhou, T. Liu, S. Liu, C. Wang, L. Guo, Nanoscale 9 (2017) 4409–4418.
[61] X. Wang, Y.V. Kolen'ko, X.-Q. Bao, K. Kovnir, L. Liu, Angew. Chem. Int. Ed. 54 (2015) 8188–8192.
[62] B. Seo, D.S. Baek, Y.J. Sa, S.H. Joo, CrystEngComm 18 (2016) 6083–6089.
[63] S. Hwang, S.H. Porter, G. Gardner, A.B. Laursen, H. Wang, M. Li, V. Amarasinghe, E. Taghaddos, A. Safari, E. Garfunkel, M. Greenblatt, G.C. Dismukes, ECS Trans. 72 (2016) 31–51.
[64] D. Merki, H. Vrubel, L. Rovelli, S. Fierro, X. Hu, Chem. Sci. 3 (2012) 2515–2525.
[65] Y. Liang, Q. Li, A.M. Asiri, X. Sun, Y. Luo, ACS Catal. 4 (2014) 4065–4069.
[66] T. Liu, X. Ma, D. Liu, S. Hao, G. Du, Y. Ma, A.M. Asiri, X. Sun, L. Chen, ACS Catal. 7 (2017) 98–102.
[67] R. Zhang, X. Wang, S. Yu, T. Wen, X. Zhu, F. Yang, X. Sun, X. Wang, W. Hu, Adv. Mater. 29 (2017) 1605502.
[68] I.K. Mishra, H. Zhou, J. Sun, F. Qin, K. Dahal, J. Bao, S. Chen, Z. Ren, Energy Environ. Sci. 11 (2018) 2246–2252.
[69] Y.-Y. Ma, C.-X. Wu, X.-J. Feng, H.-Q. Tan, L.-K. Yan, Y. Liu, Z.-H. Kang, E.-B. Wang,

Y.-G. Li, Energy Environ. Sci. 10 (2017) 788–798.

[70] C.G. Moralesguio, L.A. Stern, X. Hu, Chem. Soc. Rev. 43 (2014) 6555–6569.

[71] M.-R. Gao, J.-X. Liang, Y.-R. Zheng, Y.-F. Xu, J. Jiang, Q. Gao, J. Li, S.-H. Yu, Nat. Commun. 6 (2015) 5982.

[72] Y. Sun, C. Liu, D.C. Grauer, J. Yano, J.R. Long, P. Yang, C.J. Chang, J. Am. Chem. Soc. 135 (2013) 17699–17702.

[73] H. Li, Q. Tang, B. He, P. Yang, J. Mater. Chem. A 4 (2016) 6513–6520.

[74] X. Niu, Q. Tang, B. He, P. Yang, Electrochim. Acta 208 (2016) 180–187.

[75] Y. Zhao, Q. Tang, B. He, P. Yang, RSC Adv. 6 (2016) 93267–93274.

[76] S. Gao, G.-D. Li, Y. Liu, H. Chen, L.-L. Feng, Y. Wang, M. Yang, D. Wang, S. Wang, X. Zou, Nanoscale 7 (2015) 2306–2316.

[77] A.M. Turner, M.J. Abplanalp, R.I. Kaiser, Astrophys. J. 819 (2016) 97.

[78] Y. Sun, K. Xu, Z. Wei, H. Li, T. Zhang, X. Li, W. Cai, J. Ma, H.J. Fan, Y. Li, Adv. Mater. 30 (2018) 1802121.